Supporting Information

In situ reactive modification strategy to enhance the performance of n-i-p perovskite solar cells

Yupeng Zheng[ab], Zhenlin Zhang[ac], Shuguang Cao[ac], Shizi Luo[ac], Zhuoneng Bi[a], Victoria V. Ozerova[d], Nikita A. Slesarenko[d], Nikita A. Emelianov[d], Elena Shchurik[d], Lavrenty G. Gutsev[*de], Bala R. Ramachandran[e], Gennady L. Gutsev[f], Zhiwei Ren[g], Gang Li[g], Sergey M. Aldoshin[d], Pavel A. Troshin[*hd], Xueqing Xu[*ac]

[a] *CAS Key Laboratory of Renewable Energy, Guangdong Provincial Key Laboratory of Renewable Energy, Guangzhou Institute of Energy Conversion, Chinese Academy of Sciences, Guangzhou 510640, China*

[b] *University of Chinese Academy of Sciences, Beijing 100049, China*

[c] *School of Energy Science and Engineering, University of Science and Technology of China, Hefei 230026, China*

[d] *Federal Research Center for Problems of Chemical Physics and Medicinal Chemistry, Russian Academy of Sciences (FRC PCP MC RAS), Semenov Av. 1, Chernogolovka, Moscow Region 142432, Russia*

[e] *Institute for Micromanufacturing, Louisiana Tech University, Ruston, LA 71272, United States*

[f] *Department of Physics, Florida A&M University, Tallahassee, Florida 32307, United States*

[g] *Department of Electronic and Information Engineering, Research Institute for Smart Energy (RISE), The Hong Kong Polytechnic University, Hung Hom, Kowloon, Hong Kong, China*

[h] *Zhengzhou Research Institute of HIT, 26 Longyuan East 7th, Jinshui District, Zhengzhou, Henan Province 450000, PR China*

[*]Corresponding author

E-mail address: xuxq@ms.giec.ac.cn (X. Xu), lgutsev@outlook.com (L. G. Gutsev), troshin2003@inbox.ru (P. A. Troshin)

Materials

Phenethylammonium iodide (PEAI), phenylethylammonium trifluoroacetate (PEATFA) and phenylethylammonium acetate (PEAAc) were purchased from Xi'an Yuri Solar Co., Ltd. FTO glass was purchased from Advanced Election Technology. SnO_2 solution was purchased from Alfa Aesar and Xi'an Yuri Solar Co., Ltd. FAI, MACl, PbI_2, MABr, $PbBr_2$, tris[2-(1H-pyrazol-1-yl)-4-tert-butylpyridine]-cobalt(III)-tris[bis-(trifluoromethylsulfonyl)imide] (FK209) and Spiro-OMeTAD were purchased from Xi'an Yuri Solar Co., Ltd. RbCl, DMSO, DMF, ethyl acetate and lithium bis (trifluoromethanesulphonyl) imide (Li-TFSI) were purchased from Sigma-Aldrich. 4-tert-butylpyridine (TBP) was purchased from TCI. Acetonitrile and isopropanol was purchased from Acros. Chlorobenzene was purchased from Aladdin and Sigma-Aldrich.

Device fabrication

The fabrication method of perovskite solar cells was modified from previous reports [1-3]. The size of the FTO glass is 2 cm×2 cm. The FTO glass is ultrasonically cleaned with a mixed solution of deionized water and ITO cleaning agent (20:1), deionized water, ethanol and isopropanol respectively for 20 minutes. The FTO glass was blown dry with nitrogen. Then the FTO layer was treated in a UV-O_3 cleaner for 10 minutes. The precursor of electron transport layer was prepared by mixing original SnO_2 solution (15 wt%) with deionized water with a volume ratio of 1:2.5. 100 μL of SnO_2 solution was dropped on the FTO followed by rotating at 4000 rpm for 30 s. After spin-coating, all samples were placed on a heating plate of 100℃ for pre-heating. Then all samples were heated at 150℃ for 30 minutes and cooled down naturally. Then the SnO_2 layer was treated in a UV-O_3 cleaner for 10 minutes again. Two methods were used to fabricate perovskite films. For $FAPbI_3$ perovskite deposited by two-step method, 1.5 м PbI_2 and 1.0% RbCl were dissolved in mixed solvent of DMSO and DMF (1:9). PbI_2 solution

was spin-coated onto SnO_2 layer at 1500 rpm for 30 s and annealed at 70°C for 1 minute in the glove box. FAI and MACl were dissolved in isopropanol with a weight ratio of 90:18 to achieve the total concentration of 86.4 mg mL^{-1}. 90 μL of the solution was dropped on PbI_2 layer and then the spin-coating started immediately by rotating at 1800 rpm for 30 s in the glove box. Then the films were taken out from the glove box to ambient air with relative humidity of about 35% for annealing at 150°C for 15 minutes. After fabricating the perovskite films, the solutions of PEAI (15 mM), PEATFA (5 mM) and PEAAc (5 mM) in isopropanol were dropped on perovskite and spin-coated at 5000 rpm for 30 s in glove box. Then PEAI-, PEATFA- and PEAAc-treated films were annealed at 100°C for 3, 5 and 5 minutes respectively. For PEAI-treatment without annealing, the concentration is 30 mM. The precursor of hole transport layer was prepared by dissolving 90.0 mg of Spiro-OMeTAD, 35 μL of TBP, 21 μL of Li-TFSI solution (520 mg mL^{-1} in acetonitrile) and 11 μL of FK209 solution (300 mg mL^{-1} in acetonitrile) in 1 mL of chlorobenzene. Then the solution of Spiro-OMeTAD was dropped on perovskite and spin-coated at 4000 rpm for 20 s. The devices without electrode were put in a drying cabinet with relative humidity of about 15% and ambient temperature of 25°C for overnight oxidation of Spiro-OMeTAD. Then 80 nm of gold was evaporated as the electrode.

For new SnO_2 recipe, the SnO_2 solution in water was purchased from Yuri Solar Co., Ltd. The model of the product is 307005, which contains some potassium salt dopant. The precursor of electron transport layer was prepared by mixing original SnO_2 solution (12 wt%) with deionized water with a volume ratio of 1:1. 100 μL of SnO_2 solution was dropped on the FTO followed by rotating at 4000 rpm for 30 s. After spin-coating, all samples were placed on a heating plate of 100°C for pre-heating. Then all samples were heated at 180°C for 40 minutes and cooled down naturally.

In order to confirm the embedding of PEA^+ into perovskite, $FA_{0.95}MA_{0.05}Pb(I_{2.85}Br_{0.15})$ perovskite without obvious excess of PbI_2 were prepared by antisolvent method. FAI (1.40 M), MACl (0.50 M), PbI_2 (1.53 M), MABr (0.070 M) and $PbBr_2$ (0.070 M) were dissolved in mixed solvent of DMSO and DMF (1:8). The precursor solution was dropped onto SnO_2 layer and spin-coated at 1000 rpm for 10 s firstly and then 5000

rpm for 30 s in the glove box. After the spin-coating started for 20 s, 0.12 ml ethyl acetate was dropped on the film. The film was then annealed at 100°C for 60 minutes in glove box.

For the stability test against thermal stress, 151.4 mg FAI, 31.2 mg CsI, 461 mg PbI_2, 20.3 mg MACl and 96 μL NMP are dissolved in 500 μL DMF to form the precursor solution of $FA_{0.88}Cs_{0.12}PbI_3$ perovskite. Then the perovskite precursor solution was simply spin-coated onto SnO_2/FTO substrates in a nitrogen-filled glove box at 5000 rpm for 60 s. The films were then annealed at 70 °C for 1 minute and taken out for further annealing at 150 °C for 10 minutes in an ambient environment with a relative humidity of ~20-30%.

The precursor of PTAA solution was prepared by dissolving 30.0 mg of PTAA, 15 μL of TBP and 5 μL of Li-TFSI solution (520 mg mL^{-1} in acetonitrile) in 1 mL of chlorobenzene. Then the solution of PTAA was dropped on perovskite and spin-coated at 3000 rpm for 30 s.

Characterization

^{1}H, ^{19}F and ^{13}C nuclear magnetic resonance (NMR) spectra were collected using a Bruker 500MHz FT-NMR instrument spectrometer (Bruker, AVANCE III). DMSO-d6 was used as a solvent and the spectra were recorded at room temperature. The IR s-SNOM measurements were carried out using a neaSNOM microscope (Neaspec, Haar, Germany) in PsHet mode with a Mid-IR laser MIRcat-2400 (Daylight Solutions, USA) installed inside the MBraun glove box (O_2, H_2O < 0.1 ppm). The same microscope was utilized for KPFM measurements using Pt/Ir alloy cantilevers. X-ray photoelectron spectra (XPS) were recorded by ESCALAB 250Xi (Thermo Fisher Scientific Inc, American). X-ray diffraction (XRD) patterns were obtained using X'Pert PRO MPD X-ray diffractometer with Cu Kα irradiation at a scan rate (2θ) of 0.0167 ° s^{-1}. Grazing incidence wide-angle x-ray scattering (GIWAXS) measurements were carried out using Xeuss 2.0 (Xenocs, France) with copper target and x-ray light tube power of 30W and wavelength of 1.54189 Å. The microstructure of perovskite films and solar cells was characterized by SU-70 High resolution analytical scanning electron microscope

(Hitachi, Japan). PL and TRPL of perovskite films were measured using Edinburgh fluorescence spectrometers (FLS980). The excitation wavelength of laser was 405 nm. 100 mW/cm^2 illumination (AM 1.5G) is provided by ABET Sun 3000 solar simulator with a source meter (Keithley 2420) and calibrated by a standard silicon solar cell. The *J-V* curves and SCLC tests of the solar cells were obtained using Autolab TYPE II electrochemical work station. The EQE spectra of the solar cells were recorded by QTest Hifinity5 (Crowntech, American). Ultraviolet photoelectron spectra (UPS) were obtained using ESCALAB 250Xi (Thermo Scientific) with the HeI (21.22 eV) emission line employed for excitation. Atomic force microscopy (AFM) and Kelvin probe force microcopy (KPFM) measurements were carried out on a Bruker Multimode 8. The stability of solar cells under operational conditions was tested using Photovoltaic Performance Decay Testing System, PVLT-6001P-16A model (Suzhou D&R Instruments Co., Ltd). The contact angle measurements were done by JD-901A (DongGuan JingDing Instrument Co., Ltd).

Density functional theory

Surface-based supercell calculations were performed with the The Vienna Ab initio Simulation Package (VASP) of programs [4]. For simplicity, the α-$FAPbI_3$ surface was cut along the Miller index (100) and used as the reference for all calculations were followed. Two terminal types were chosen: the PbI_2-rich surface, which has only PbI_2 exposed at both surface terminals and the FAI-rich surface. To simplify the discussion of results we consider the (100) direction as the "z-axis". Relatively large supercells with a dimension of 3x3x5 allowed us to sufficiently isolate passivants from mirror image interactions. 20 Å of vacuum were included in the calculation and a full relaxation of atomic and lattice constants was allowed; however, with the constraint of the cell volume remaining constant.

A PBE functional [5] was combined with D3 dispersion correction [6]. It has been found that this combination of GGA functional and dispersion correction demonstrates good agreement with the experimental lattice constants of $CsPbI_3$ and $RbPbI_3$ and has a fortuitous error cancellation of the self-interaction error and a lack of Spin Orbit

Coupling in SOC-free calculations [7]. This allows for the prediction of band gaps with accuracy which is unusually good when compared to GGA DFT calculations of other semiconductors. Also, it was demonstrated that the PBE+D3 method presents a reasonable compromise for calculating defect formation energies [8]. All calculations were performed in the gamma-point, the projector augmented-wave (PAW) pseudopotentials [9, 10] with a plane-wave component energy cut-off of 520 eV. Also, the non-spherical contributions to the gradient inside of the PAW spheres. This correction has been shown to considerably improve the accuracy of simulated observables of perovskite oxides [11].

The adsorption energies were calculated as:

$$E_{ads}(D^q) = E_{perovsk/pass}(D^q) - E_{perovsk}(D^q) - E_{pass} \quad (2)$$

Where D^q in the case of the PbI_2-rich perovskite is the Pb_I anti-site defect. In the case of FAI-rich surface we considered either the defect V_{FAI} when passivating with PEAX (X=I, TFA, Ac) or V_{FA} when considering only PEA passivation. $E_{perovsk/pass}$ is the energy of the surface with passivant added, $E_{perovsk}$ is the passivant-free surface and E_{pass} is the energy of the passivant in either gas phase or from FAX (X=I, TFA, Ac) in the case of the moderate and Pb-rich regimes. The work function was measured from the halfway point of the vacuum between the periodic layers, it was observed not to change much; however, the slope of the change of the coulombic potentiall in vacuum dV/dz did change (more details in SI).

The molecular Electrostatic Potential Surfaces (MESP's) were calculated with the GAUSSIAN 09 suite of programs[1] and then plotted with Gaussview. The hybrid B3LYP functional was utilized along with a triple-ζ quality 6-311++G* basis set along and a D3 dispersion correction.

Supplementary Notes

Supplementary Note 1: Detailed analysis of the chemical environment of AcO^- anions in different systems.

The characteristic peaks of AcO^- anions in the ^1H NMR spectra of PEAAc, PEAAc + FAI, $Pb(OAc)_2$, PEAAc + PbI_2 and PEAAc + PbI_2 + FAI systems are located at δ of 1.820, 1.777, 1.685, 1.729 and 1.723 ppm, respectively. Therefore, the chemical environment of AcO^- anions in PEAAc + PbI_2 and PEAAc + PbI_2 + FAI systems is obviously closer to that of $Pb(OAc)_2$ system than that of PEAAc system.

Furthermore, the NMR spectra of the triple-component PEAAc + PbI_2 + FAI system unambiguously revealed the formation of $Pb(OAc)_2$ and PEAI, whereas the interaction of PEAAc with FAI has been completely suppressed.

To sum up, AcO^- anions tend to bind Pb^{2+} cations than the other organic cations due to the strong affinity of AcO^- anions to Pb^{2+} cations. Therefore, $Pb(OAc)_2$ is quite likely to form on the surface of PEAAc-modified perovskite films.

Supplementary Note 2: The factors affecting the intensity of N 1s peak at about 400.8 eV of PEAX-modified perovskite films.

There are two factors affecting the intensity of N 1s peak at about 400.8 eV of PEAX-modified perovskite films. Firstly, the concentrations of PEAI, PEATFA and PEAAc used are 15, 5 and 5 mM, respectively. These concentrations are selected to achieve the best photovoltaic performance of solar cells. The higher concentration of PEAI should contribute to stronger intensity of N 1s peak at about 400.8 eV of PEAI-modified perovskite films to some extent.

Secondly, another factor should be PEAX's ability to provide PEA^+ to intercalate into the perovskite. As can be seen in the XRD patterns in Fig. 4b and Fig. 7d, when the perovskite films were treated with the solutions of PEAX in isopropanol (50 mM), the PEAI-modified perovskite always show stronger diffraction peaks belonging to two-dimensional perovskite. Therefore, PEAI shows the strongest ability to provide PEA^+ to intercalate into perovskite, which also increases the intensity of N 1s peak at about 400.8 eV. This factor should also account for the stronger intensity of N 1s peak at about 400.8 eV of PEATFA-modified films than that of PEAAc-modified films. Because PEATFA is more inclined to provide PEA^+ to intercalate into perovskite. This situation is similar to the case in the paper entitled “Engineering ligand reactivity

enables high-temperature operation of stable perovskite solar cells" published in **Science**.[12] In the paper, the mass concentrations of octylammonium iodide (OAI) and anilinium iodide (AnI) used for surface passivation are the same, but the intensity of N 1s peak belonging to ammonium ligands of OAI is about four times that of AnI. The reason is that OA^+ diffused into the perovskites more easily.

Supplementary Note 3: The reasons for the small red shift of PL of PEAX-modified perovskite films.

The small red shift of PL of PEAX-modified perovskite films could be attributed to the consumption of the excess of PbI_2, the dielectric confinement provided by 2D perovskite or the structural changes of perovskite caused by the embedding of cations or anions of PEAX.[2, 13-17]

(1) Consuming the excess of PbI_2 can narrow the band gap of perovskite by suppressing the strong quantum confinement in perovskite/PbI_2.[2]

(2) The dielectric confinement occurred between 3D perovskite and 2D perovskite would reduce the optical band gap (E_{opt}) of 3D perovskite if the electrical band gap (E_g) of 3D perovskite does not change.[13]

(3) The red shift of PL could also be attributed to the structural changes of perovskite caused by the embedding of cations or anions of passivators or additives.[14-17] For instance, such phenomenon has been observed by the embedding of K^+, FA^+ and I^- into $MAPbI_3$, respectively.[14-17]

Figures and tables

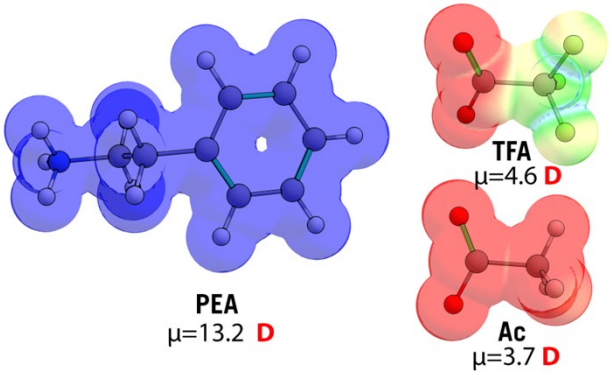

Fig. S1. Gas phase dipole moments of PEA^+, Ac^- and TFA^-.

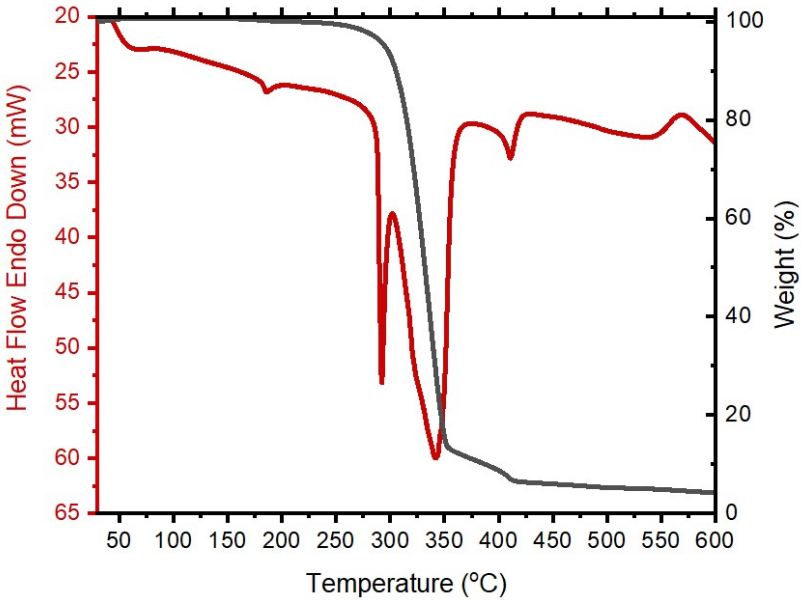

Fig. S2. Differential thermal analysis data for PEAI: weight loss (black) and differential scanning calorimetry curve (red).

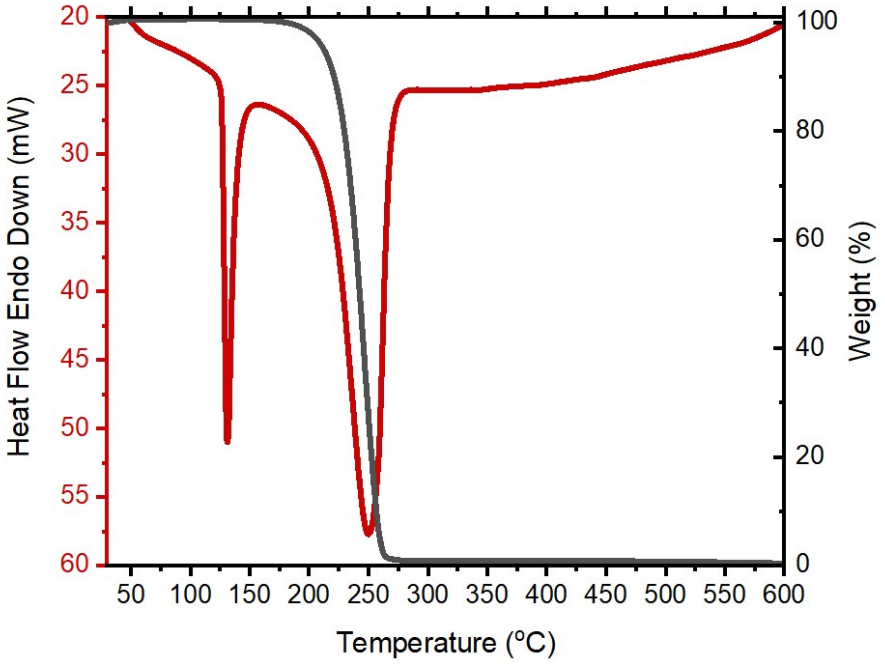

Fig. S3. Differential thermal analysis data for PEATFA: weight loss (black) and differential scanning calorimetry curve (red).

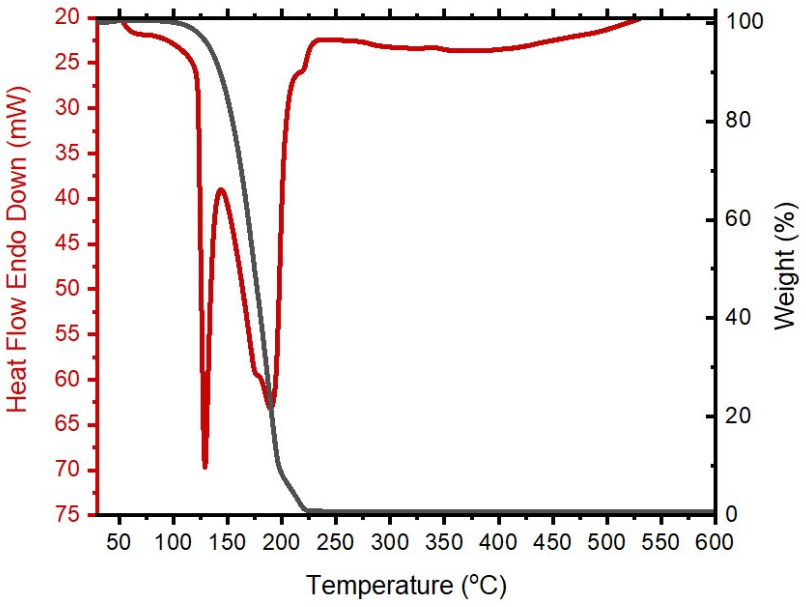

Fig. S4. Differential thermal analysis data for PEAAc: weight loss (black) and differential scanning calorimetry curve (red).

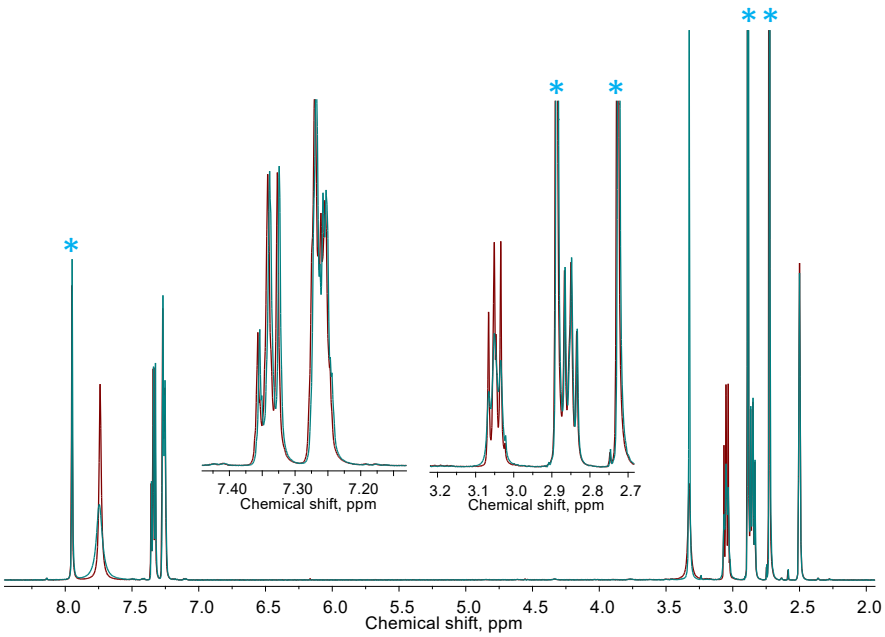

Fig. S5. Comparison of the ^{1}H NMR spectra of PEAI + PbI_2 solution (cyan) and pristine PEAI solution (red-brown) in DMSO-D6. Symbols "*" denote signals of DMF internal reference.

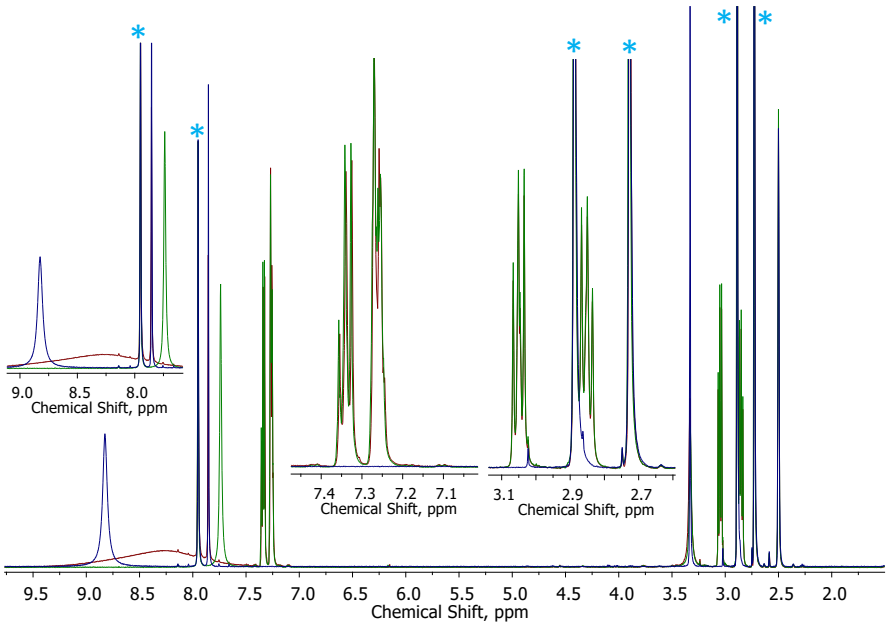

Fig. S6. Comparison of the ^{1}H NMR spectra of PEAI + FAI solution (red-brown) and pristine PEAI (green) and FAI (blue) solutions in DMSO-D6. Symbols "*" denote signals of DMF internal reference.

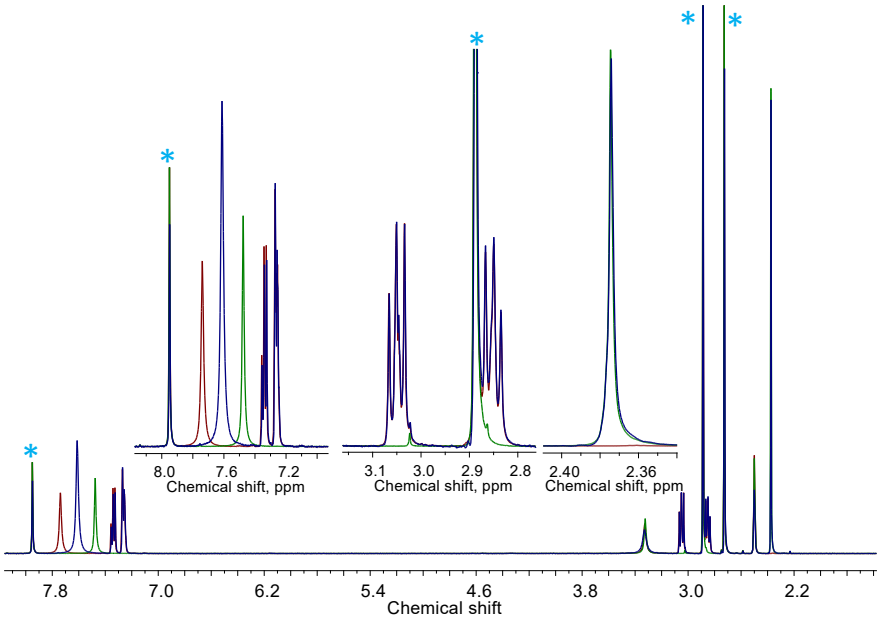

Fig. S7. Comparison of the ^{1}H NMR spectra of PEAI + MAI solution (blue) and pristine PEAI (red-brown) and MAI (green) solutions in DMSO-D6. Symbols "*" denote signals of DMF internal reference.

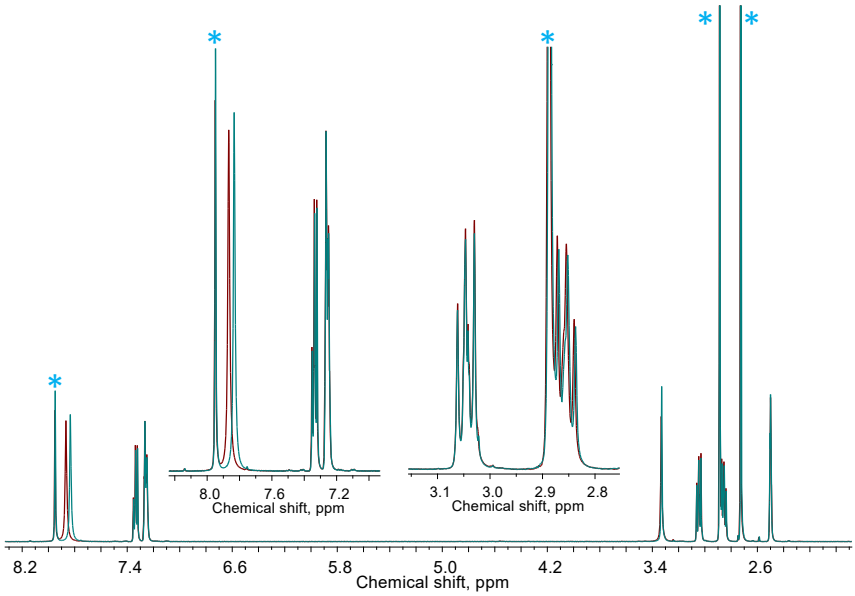

Fig. S8. Comparison of the ^{1}H NMR spectra of PEATFA + PbI_2 solution (cyan) and pristine PEATFA solution (red-brown) in DMSO-D6. Symbols "*" denote signals of DMF internal reference.

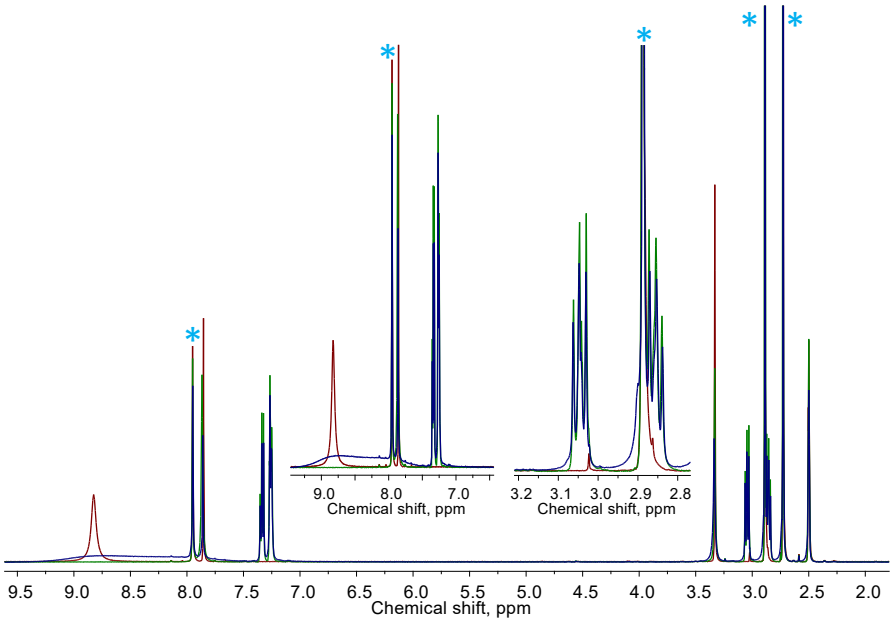

Fig. S9. Comparison of the ^{1}H NMR spectra of PEATFA + FAI solution (blue) and pristine PEATFA (green) and FAI (red-brown) solutions in DMSO-D6. Symbols "*" denote signals of DMF internal reference.

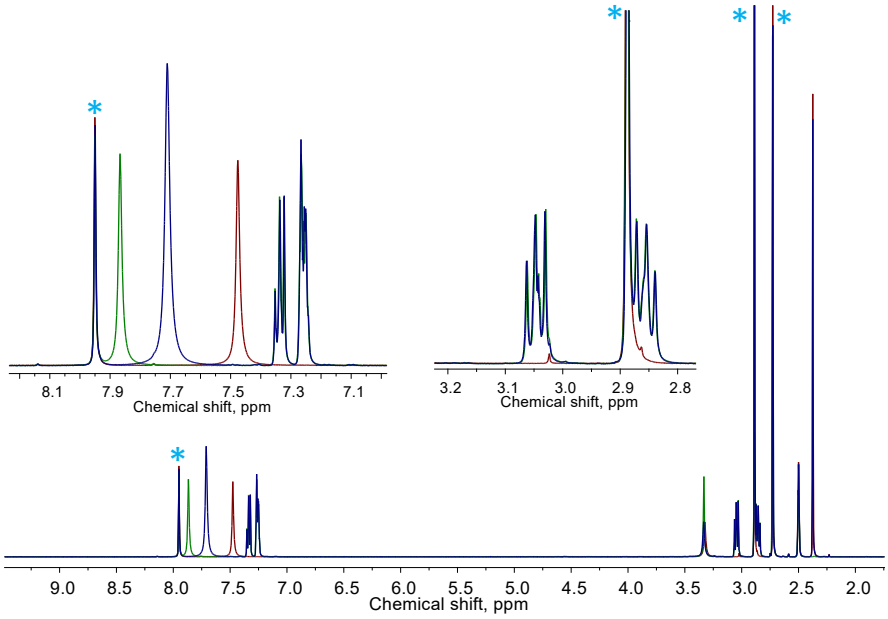

Fig. S10. Comparison of the ^{1}H NMR spectra of PEATFA + MAI solution (blue) and pristine PEATFA (green) and MAI (red-brown) solutions in DMSO-D6. Symbols "*" denote signals of DMF internal reference.

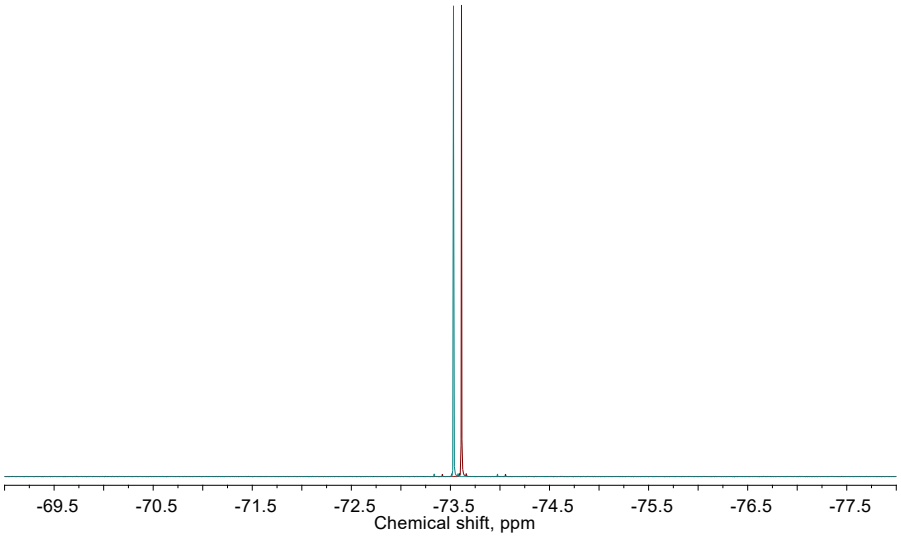

Fig. S11. Comparison of the ^{19}F NMR spectra of PEATFA + PbI_2 solution (red-brown) and pristine PEATFA solution (cyan) in DMSO-D6.

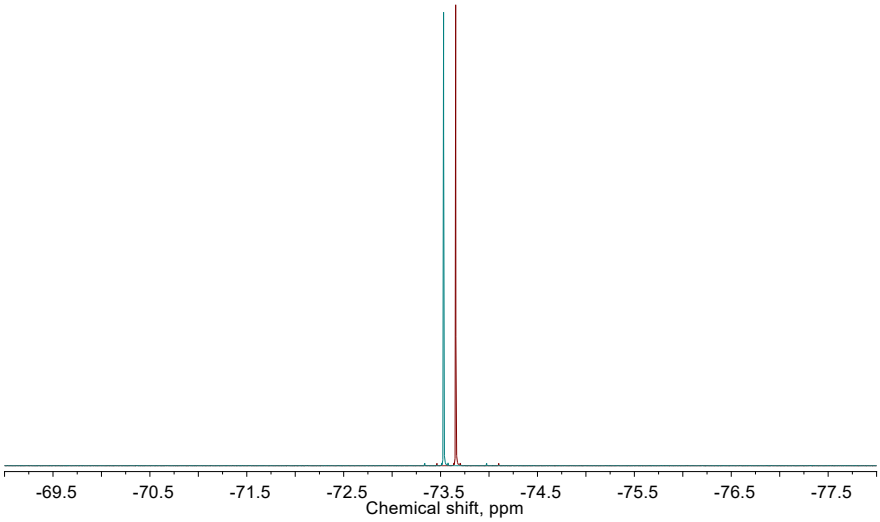

Fig. S12. Comparison of the ^{19}F NMR spectra of PEATFA + FAI solution (red-brown) and pristine PEATFA solution (cyan) in DMSO-D6.

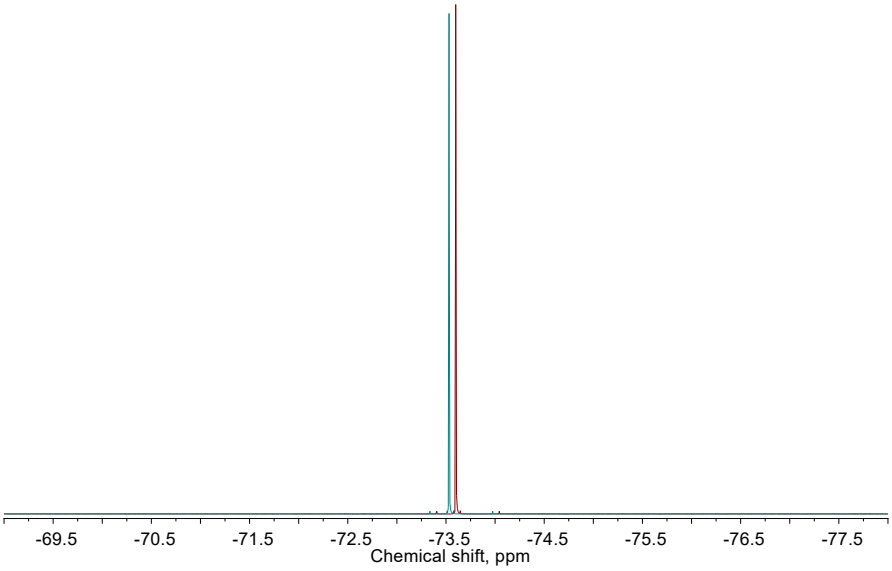

Fig. S13. Comparison of the ^{19}F NMR spectra of PEATFA + MAI solution (red-brown) and pristine PEATFA solution (cyan) in DMSO-D6.

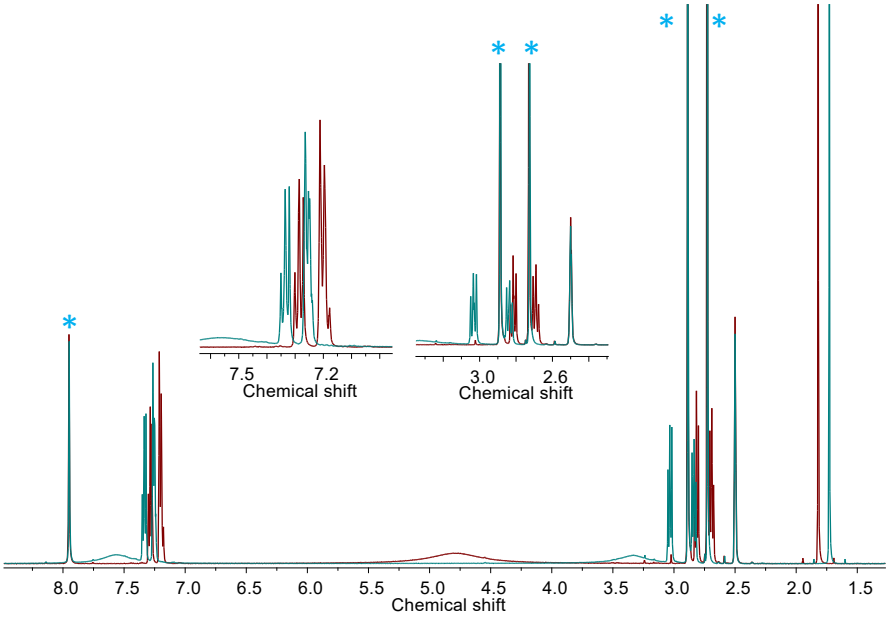

Fig. S14. Comparison of the ^{1}H NMR spectra of PEAAc + PbI_2 solution (cyan) and pristine PEAAc solution (red-brown) in DMSO-D6. Symbols "*" denote signals of DMF internal reference.

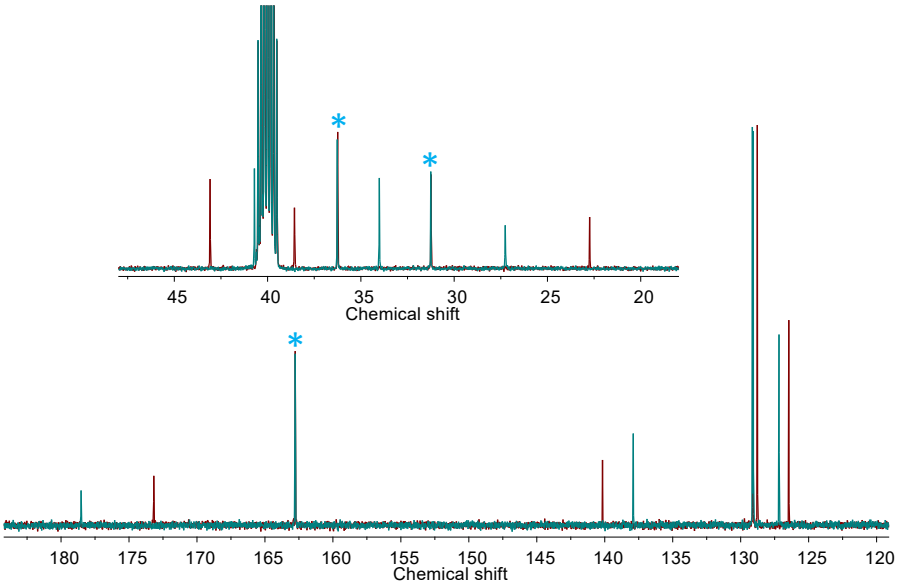

Fig. S15. Comparison of the ^{13}C NMR spectra of PEAAc + PbI_2 solution (cyan) and pristine PEAAc solution (red-brown) in DMSO-D6. Symbols "*" denote signals of DMF internal reference.

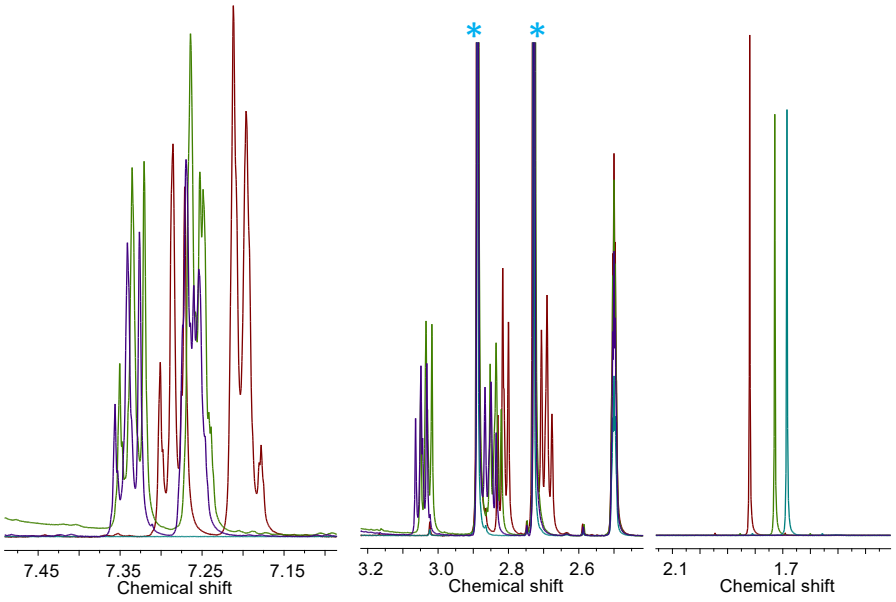

Fig. S16. Comparison of the characteristic fragments of ^{1}H NMR spectra of PEAAc + PbI_2 solution (olive) with pristine solutions of PEAAc (red-brown), PEAI (violet) and $Pb(OAc)_2$ (cyan) in DMSO-D6. Symbols "*" denote signals of DMF internal reference.

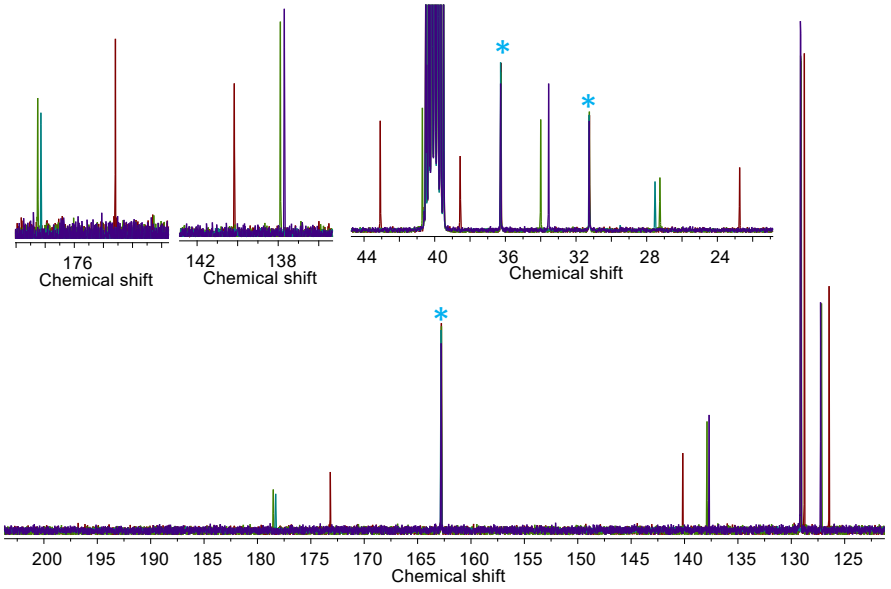

Fig. S17. Comparison of the characteristic fragments of the ^{13}C NMR spectra of PEAAc + PbI_2 solution (olive) with pristine solutions of PEAAc (red-brown), PEAI (violet) and $Pb(OAc)_2$ (cyan) in DMSO-D6. Symbols "*" denote signals of DMF internal reference.

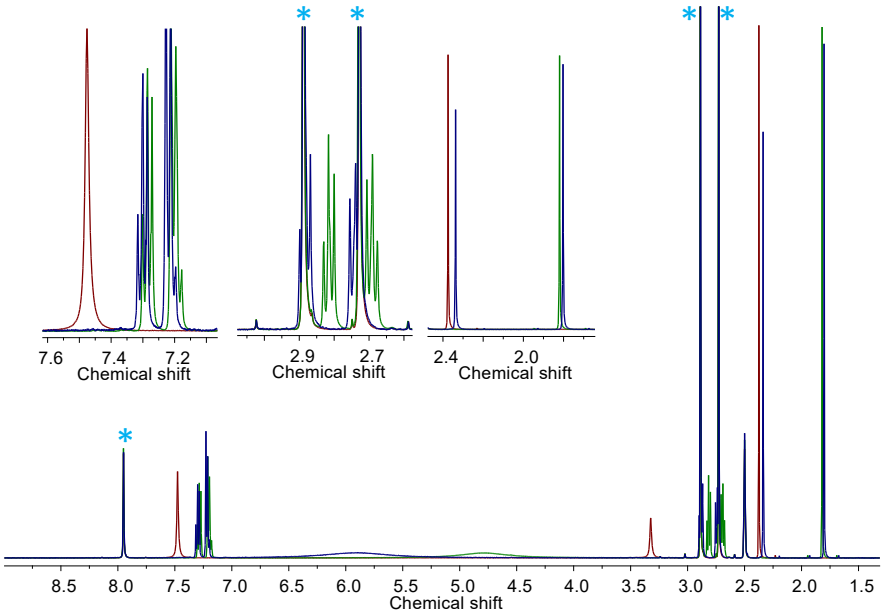

Fig. S18. Comparison of the ^{1}H NMR spectra of PEAAc + MAI solution (blue) with pristine solutions of MAI (red-brown) and PEAAc (green) in DMSO-D6. Symbols "*" denote signals of DMF internal reference.

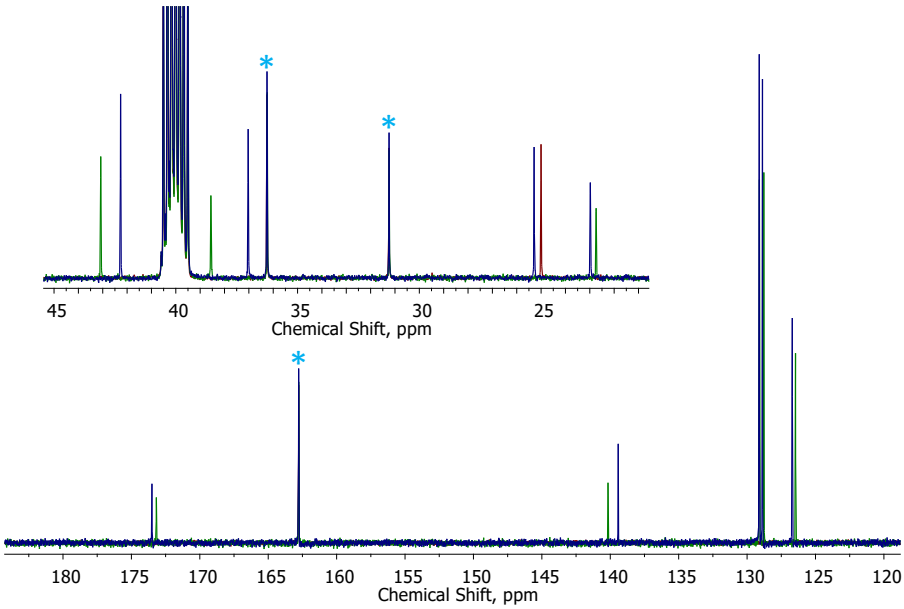

Fig. S19. Comparison of the ^{13}C NMR spectra of PEAAc + MAI solution (blue) with pristine solutions of MAI (red-brown) and PEAAc (green) in DMSO-D6. Symbols "*" denote signals of DMF internal reference.

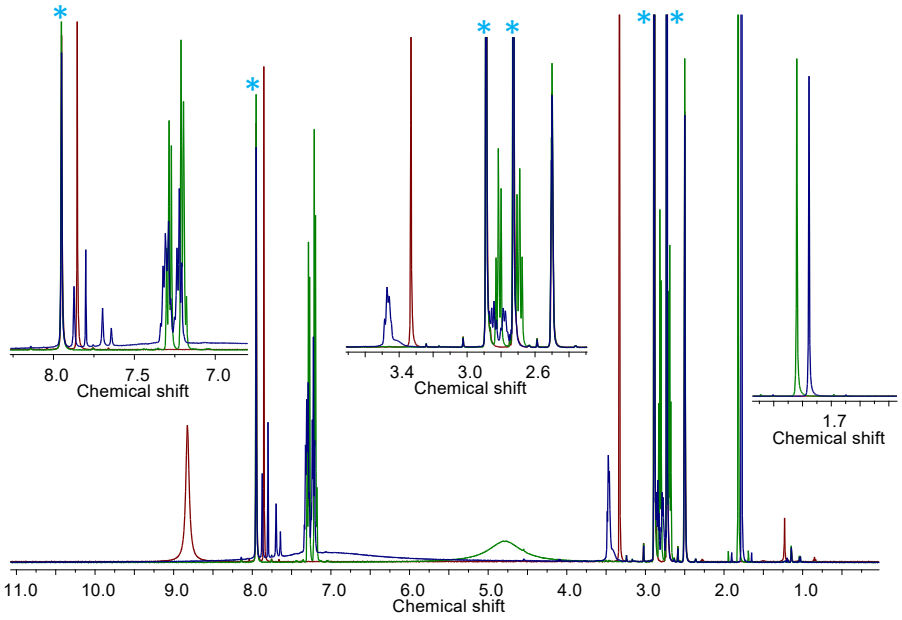

Fig. S20. Comparison of the ^{1}H NMR spectra of PEAAc + FAI solution (blue) with pristine solutions of FAI (red-brown) and PEAAc (green) in DMSO-D6. Symbols "*" denote signals of DMF internal reference.

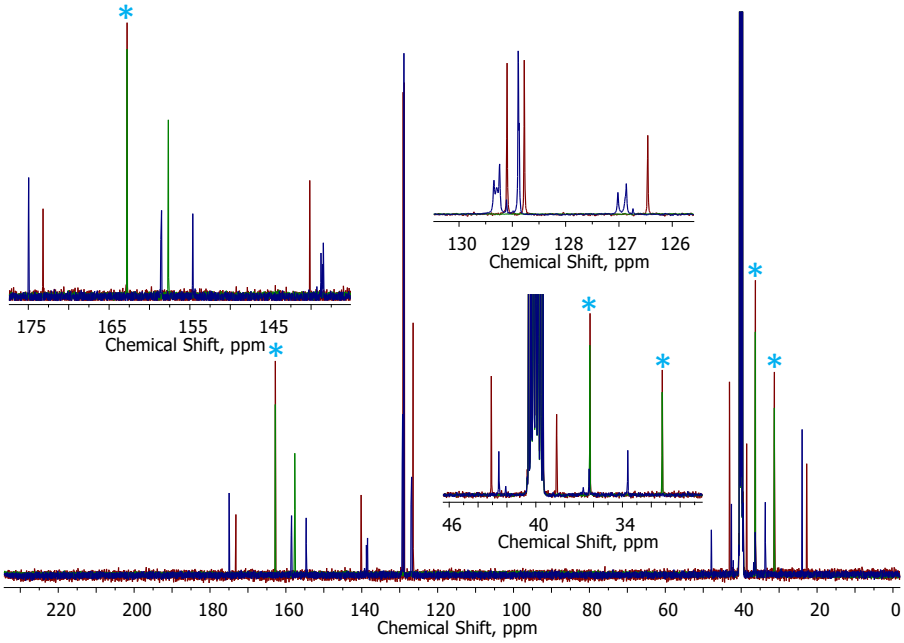

Fig. S21. Comparison of the ^{13}C NMR spectra of PEAAc + FAI solution (blue) with pristine solutions of FAI (green) and PEAAc (red-brown) in DMSO-D6. Symbols "*" denote signals of DMF internal reference.

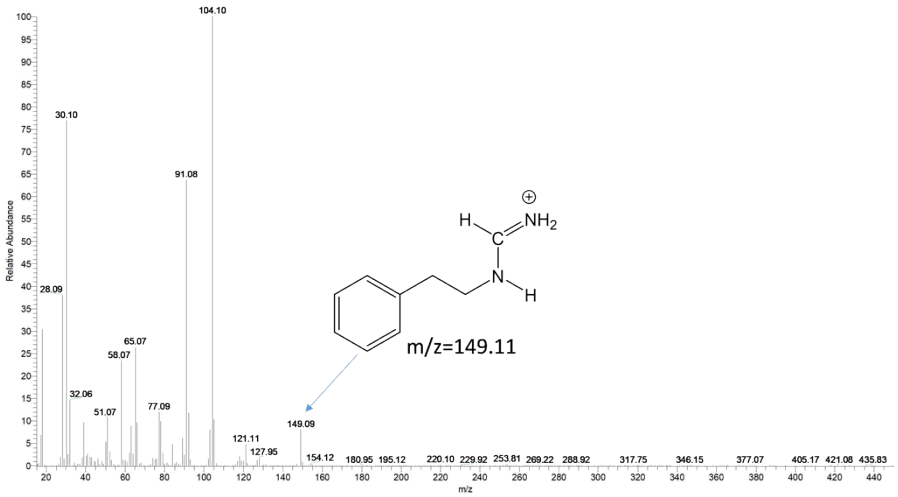

Fig. S22. EI mass spectrum of the first reaction product of PEAAc with FAI (GC retention time 16.53 min) showing molecular ion with m/z=149 (A and/or B) and a set of fragmentation ions.

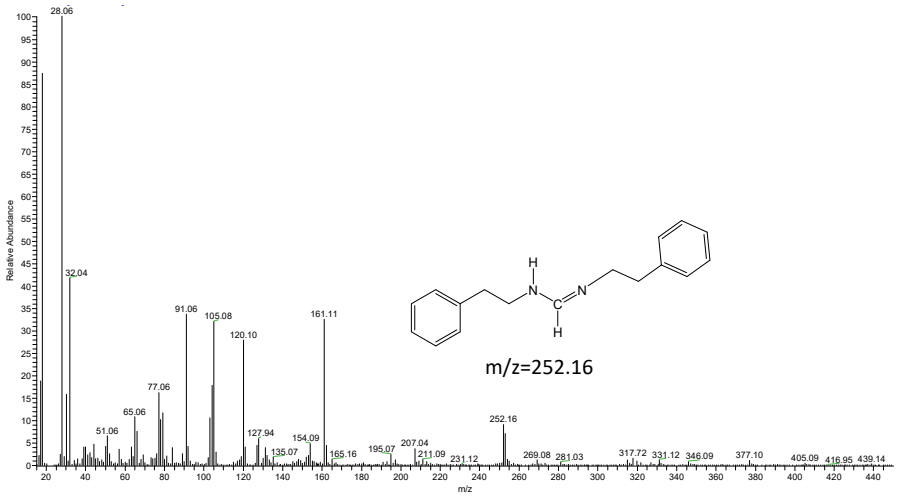

Fig. S23. EI mass spectrum of the second reaction product of PEAAc with FAI (GC retention time 26.00 min) showing molecular ion with m/z=252 (corresponds to product C) and a set of fragmentation ions.

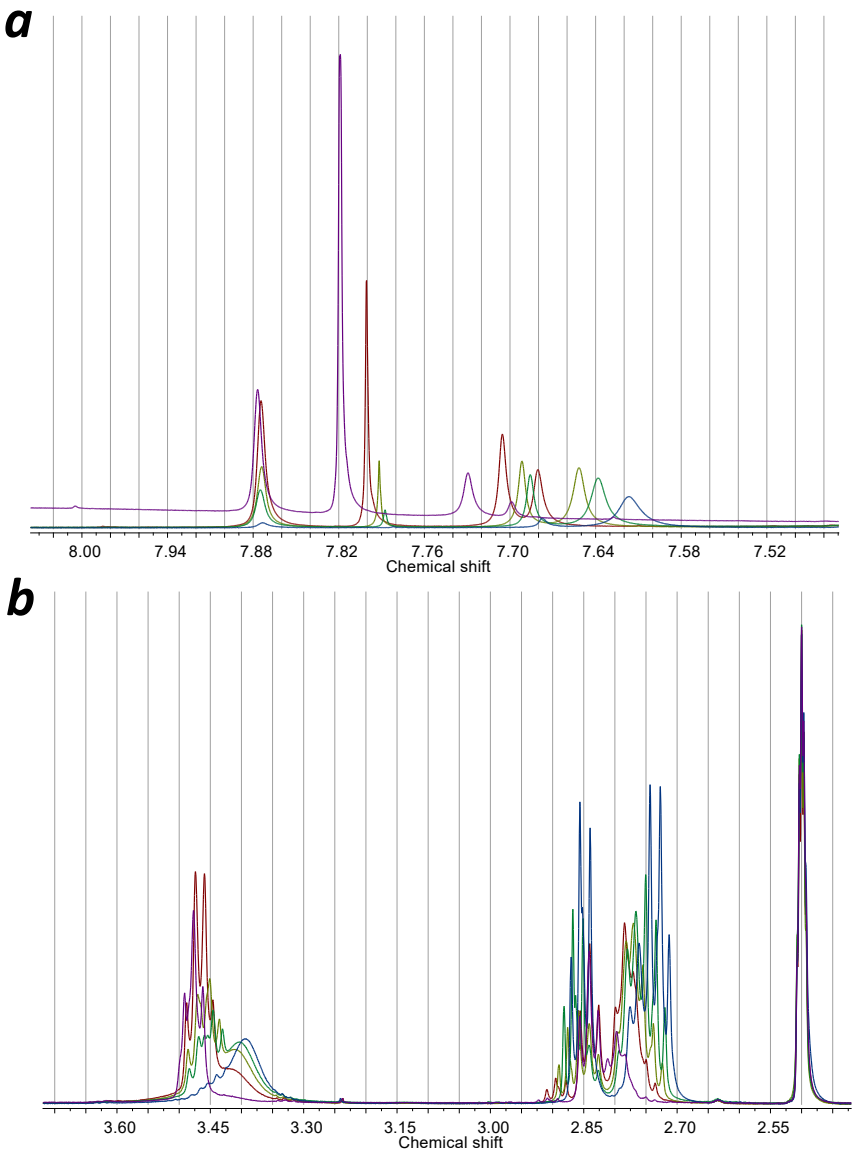

Fig. S24. Comparison of the ^{1}H NMR spectra of the samples obtained by mixing PEAAc and FAI in different molar ratios: 1:2 (violet), 1:1 (dark red), 1:0.66 (olive), 1:0.5 (green) and 1:0.25 (blue). All solutions prepared in DMSO-D6.

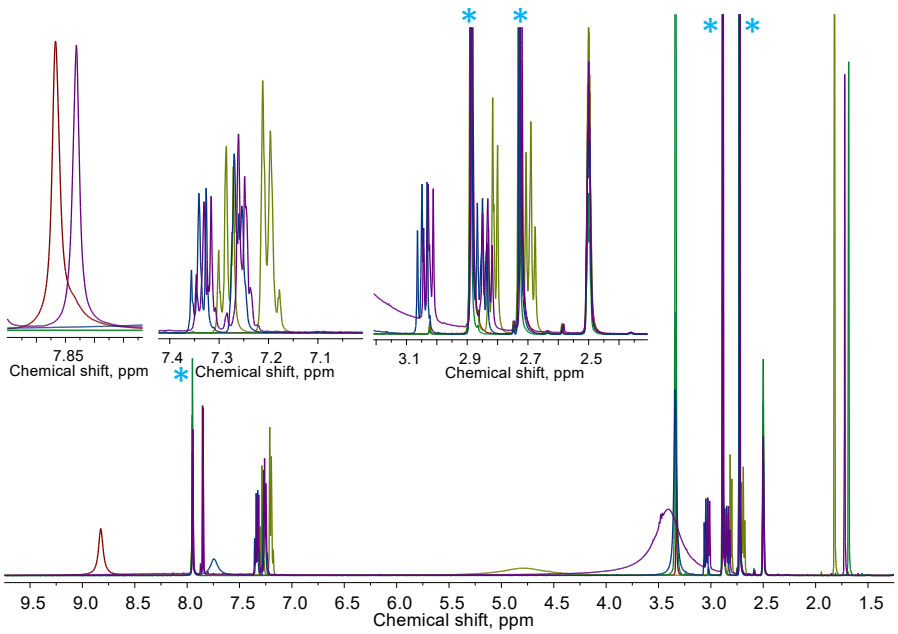

Fig. S25. Comparison of the characteristic fragments of ^{1}H NMR spectra of PEAAc + PbI_2 + FAI solution (violet) with pristine solutions of PEAAc (olive), PEAI (bluer) and $Pb(OAc)_2$ (green) in DMSO-D6. Symbols "*" denote signals of DMF internal reference.

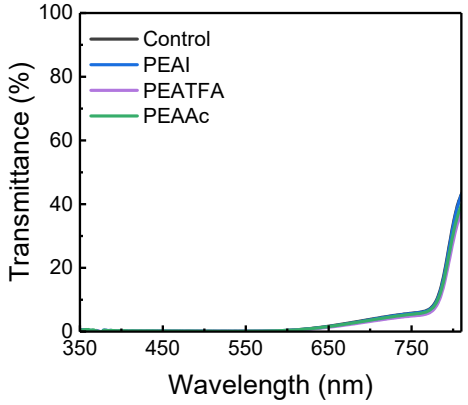

Fig. S26. The transmittance of the control and PEAX-treated perovskite films, where X=I, TFA and Ac.

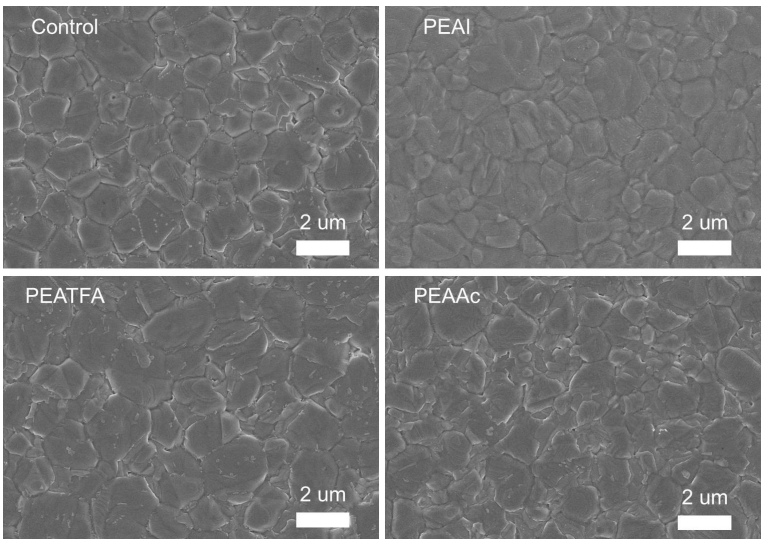

Fig. S27. The morphology of the control and PEAX-treated perovskite films as revealed by scanning electron microscopy (SEM).

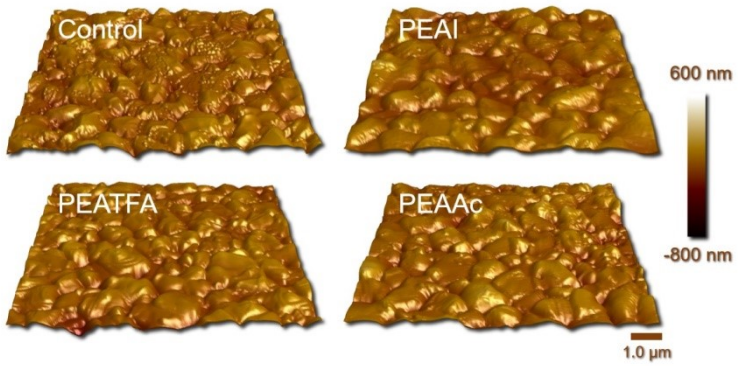

Fig. S28. The morphology of the control and PEAX-modified perovskite films as revealed by atomic force microscopy (AFM). The root mean square (RMS) roughness of the control, PEAI-, PEATFA- and PEAAc-modified perovskite films are 50.1, 51.5, 49.3 and 49.5 nm, respectively.

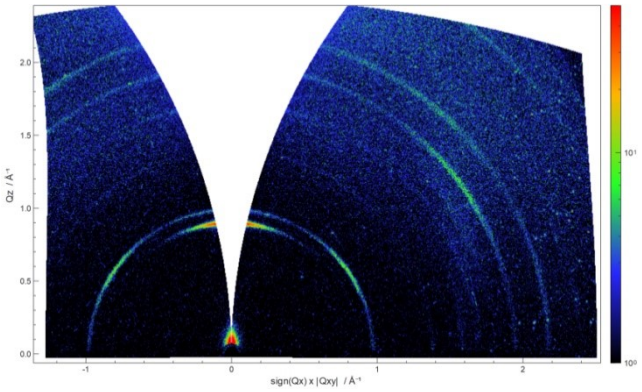

Fig. S29. The surface structure of PEATFA-treated perovskite characterized by grazing incidence wide-angle x-ray scattering (GIWAXS).

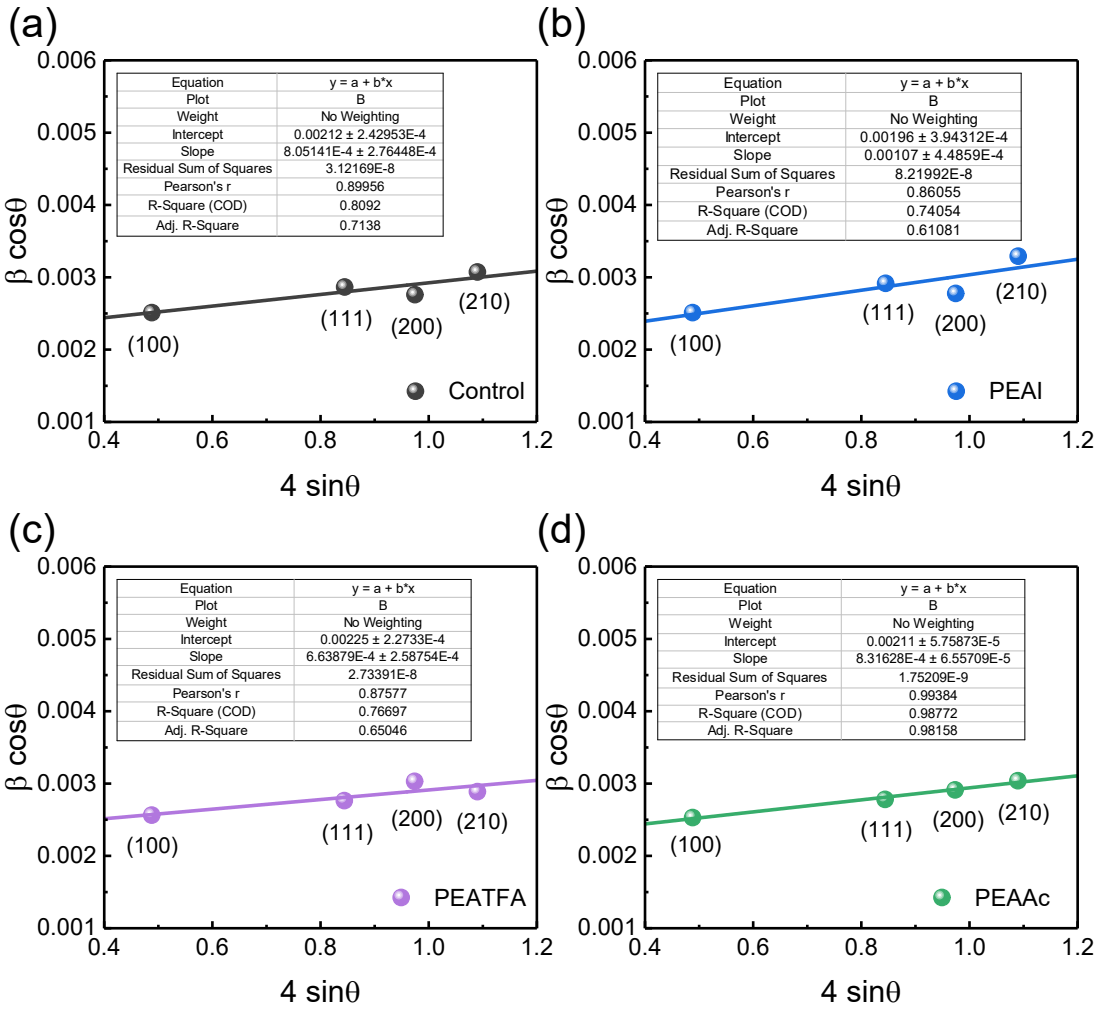

Fig. S30. Williamson-Hall plots of the control and PEAX-modified perovskite films based on the XRD patterns.

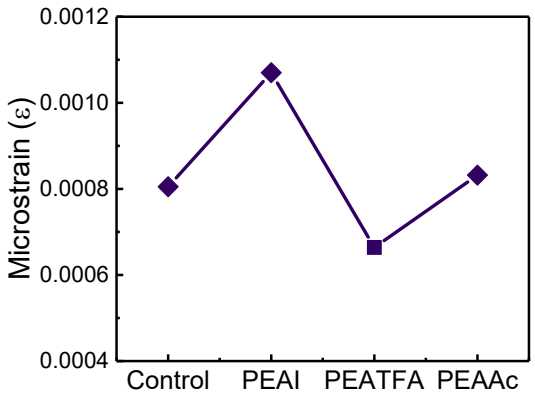

Fig. S31. The extracted lattice strain of the control and PEAX-modified perovskite films from the Williamson-Hall plots.

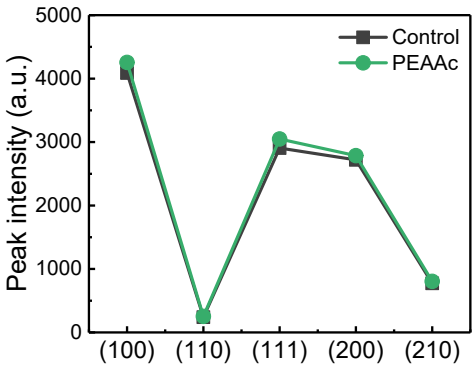

Fig. S32. The peak intensity of the diffraction peaks of α-phase perovskite in the control and PEAAc-modified films.

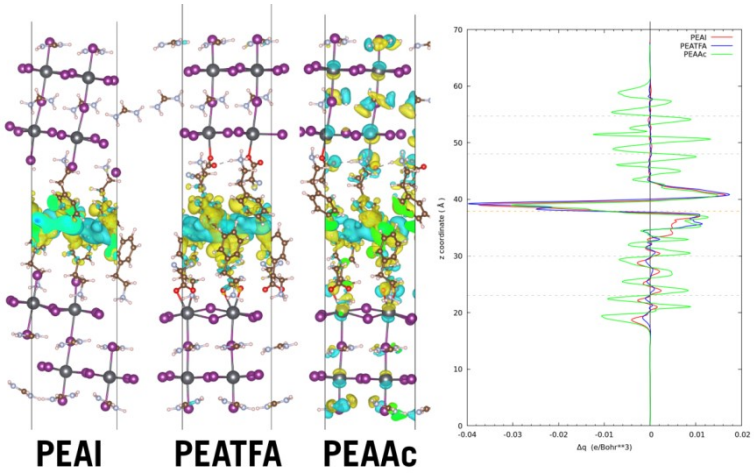

Fig. S33. (left) The interfacial charge distribution of three kinds of 2D perovskite interlayers. 3D plots of the charge density difference Δρ of the PEAI, PEATFA and PEAAc 2D-3D perovskite interfaces and the (right) averaged planar density difference projected onto the long z-axis, the orange dotted line represents the center point of the interface. Note the larger variations in the 3D-perovskite lattice in the case of PEAAc which implies a stronger induced dipole effect.

Fig. S34. The surface potential distribution and work function (WF) of control and PEAX-treated perovskite films characterized by KPFM.

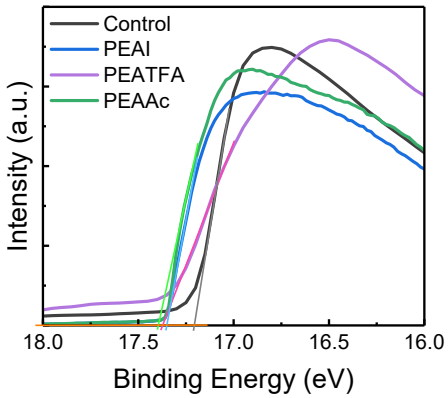

Fig. S35. The work function of perovskite films recorded by ultraviolet photoelectron spectroscopy (UPS). The valence band maximum difference (ΔE_{VBM}) between the three-dimensional perovskite (5.39 eV) and PEA_2PbI_4 (5.71 eV) is about -0.32 eV.

Table S1. Overview of spectral changes induced by mixing PEAI with different perovskite precursor components (numbering of the atoms is shown on the Figure ST1 below).

System / Atoms	PEAI	PEAI+PbI_2	PEAI+FAI	FAI	PEAI+MAI	MAI
H_a	7.26	7.26	7.26	-	7.26	-
H_b	7.34	7.34	7.34	-	7.34	-
H_c	7.26	7.26	7.26	-	7.26	-
H_d	2.85	2.85	2.85	-	2.85	-
H_e	3.05	3.05	3.05	-	3.05	-
H_f	7.74	7.74	8.21 (br. s)	-	7.61	-
FAI N-H	-	-	8.21 (br. s)	8.83 (br. s)	-	-
FAI C-H	-	-	7.85	7.85	-	-
MAI CH_3	-	-	-	-	2.37	2.37
MAI NH_3	-	-	-	-	7.61	7.48

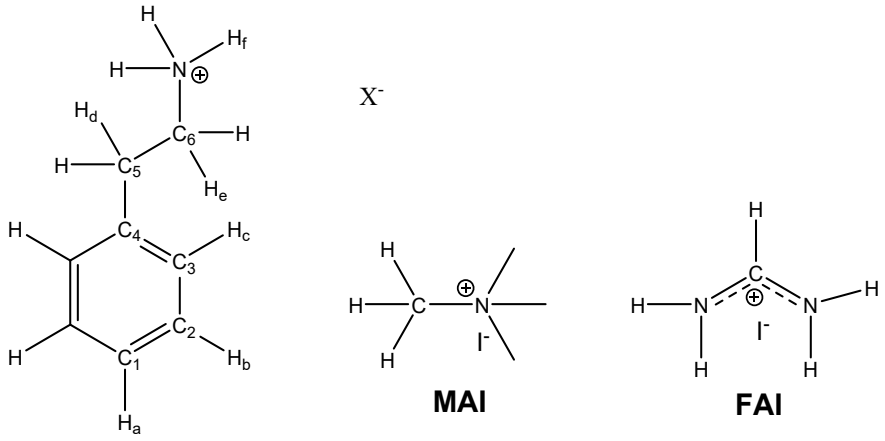

Fig. ST1. Numbering of atoms on the structure of PEAX and representations of the molecular structures of MAI and FAI

Table S2. Overview of spectral changes induced by mixing PEATFA with different perovskite precursor components (numbering of the atoms is shown on the Figure ST1 above).

System / Atoms	PEATFA	PEATFA + PbI_2	PEATFA + FAI	FAI	PEATFA + MAI	MAI
H_a	7.26	7.26	7.26		7.26	
H_b	7.34	7.34	7.34		7.34	
H_c	7.26	7.26	7.26		7.26	
H_d	2.85	2.85	2.85		2.85	
H_e	3.05	3.05	3.05		3.05	
H_f	7.87	7.83	8.76 (br. s)		7.71	
FAI N-H			8.76 (br. s)	8.83 (br. s)		
FAI C-H			7.86	7.85		
MAI CH_3					2.37	2.37
MAI NH_3					7.71	7.48
CF_3COO^-	-73.53	-73.61	-73.66	-	-73.60	-

Table S3. Overview of spectral changes induced by mixing PEAAc with different perovskite precursor components (numbering of the atoms is shown on the Figure ST1 above).

System / Atoms	PEAAc	PEAAc + PbI_2	PEAI	$Pb(OAc)_2$	PEAAc + FAI *	PEAAc + FAI + PbI_2	FAI	PEAAc + MAI	MAI
H_a	7.20	7.26	7.26	-		7.26	-	7.21	-
H_b	7.29	7.34	7.34	-		7.33	-	7.30	-
H_c	7.20	7.26	7.26	-		7.26	-	7.21	-
H_d	2.69	2.84	2.85	-		2.83	-	2.74	-
H_e	2.82	3.03	3.05	-		3.03	-	2.89	-
H_f	4.78	7.58	7.74	-		3.40	-	5.95	-
CH_3COO^-	1.82	1.73	-	1.69		1.72	-	1.83	-
FAI N-H	-	-	-	-		8.14 (br. s)	8.83 (br. s)	-	-
FAI C-H	-	-	-	-		7.85	7.85	-	-
MAI CH_3	-	-	-	-	-		-	2.34	2.37
MAI NH_3	-	-	-	-	-		-	5.95	7.48
C_1	126.46	127.18	127.27	-			-	126.69	-
C_2	129.10	129.14	129.15	-			-	129.11	-
C_3	128.78	129.09	129.12	-			-	128.87	-
C_4	140.16	137.90	137.70	-			-	139.42	-
C_5	38.58	34.01	33.56	-			-	37.03	-
C_6	43.08	40.71	40.51	-			-	42.27	-
$\underline{C}H_3COO^-$	22.74	27.26	-	27.53			-	22.98	-
$CH_3\underline{C}OO^-$	173.18	178.52	-	178.30			-	173.50	-
MAI $\underline{C}H_3$	-	-	-	-			-	25.29	25.00

* - chemical reaction between PEAAc and FAI produces several products

Table S4. The evolution of the product composition upon change in the PEAAc: FAI molar ratio (the amount of the underacted FAI is also presented)

Component	Characteristic chemical shift	PEAAc : FAI molar ratio				
		1: 2	1:1	1:0.66	1 : 0.5	1 : 0.25
FAI	7.80	0.44	0.26	0.10	0.04	0.00
A	7.87	0.33	0.33	0.26	0.22	0.05
B	7.71	0.14	0.25	0.26	0.26	0.11
C	7.68	0.10	0.16	0.37	0.48	0.84

Table S5. The effect of PEAI-treatment without annealing on the photovoltaic performance of PSCs.

		V_{OC} (V)	J_{SC} (mA cm^{-2})	FF (%)	PCE (%)
Control	Statistic	1.15±0.01	25.8±0.3	69.7±4.4	20.7±1.3
	Champion	1.16	25.8	75.2	22.6
PEAI w/o annealing	Statistic	1.17±0.01	26.0±0.2	74.4±1.7	22.6±0.5
	Champion	1.18	26.0	75.3	23.0

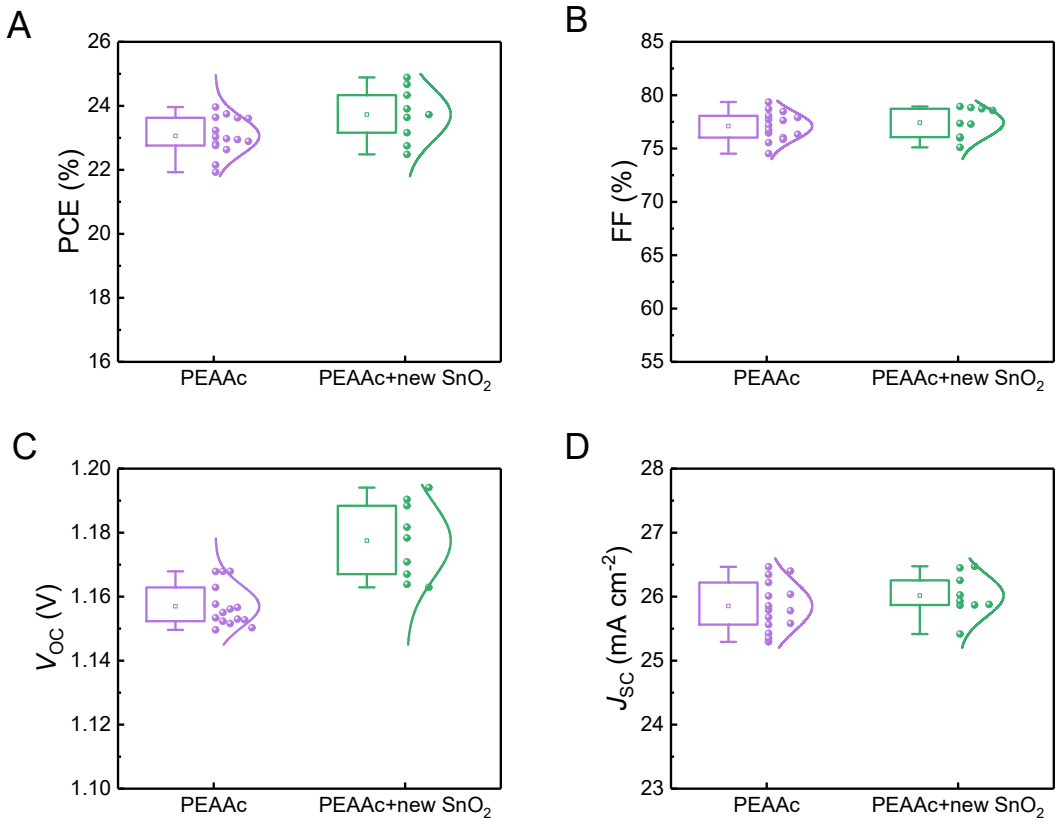

Fig. S36. Box-plots of the PCE, FF, V_{OC} and J_{SC} of PEAAc-modified PSCs with and without new SnO_2 recipe.

Table S6. Statistics of photovoltaic parameters of PEAAc-modified PSCs with and without new SnO_2 recipe.

		V_{OC} (V)	J_{SC} (mA cm^{-2})	FF (%)	PCE (%)
PEAAc	Statistic	1.16±0.01	25.9±0.4	77.1±1.3	23.1±0.6
	Champion	1.17	25.9	79.4	24.0
PEAAc + new SnO_2	Statistic	1.18±0.01	26.0±0.3	77.4±1.4	23.7±0.8
	Champion	1.19	26.5	78.7	24.9

DFT phase diagram

To define the chemical potentials within which the perovskite phase we use the following boundary conditions to define phase diagram:

$$\mu_{FA} + \mu_{Pb} + 3\mu_I = \Delta H_f(FAPbI_3) \quad (1)$$

$$\mu_{Pb} + 2\mu_I < \Delta H_f(PbI_2) \quad (2)$$

$$\mu_{FA} + \mu_I < \Delta H_f(FAI) \quad (3)$$

$$\mu_{FA} = \frac{1}{2}\mu_{H^2} + \mu_{FA-H} \quad (4)$$

$$\mu_{FA} < 0, \mu_{Pb} < 0, \mu_I < 0 \quad (5)$$

By calculating all of the relevant quantities we obtained a μ_{Pb} versus μ_I phase diagram plot (Figure S9) and chose the customary 3 points (I-rich, moderate, Pb-rich) as representative cases.

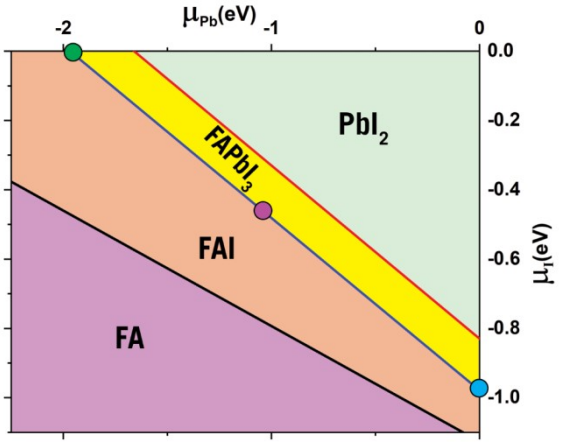

Fig. S37. The calculated phase diagram of FA-Pb-I systems with the PBE+D3 functional. Three symbols in (a) represent the I-rich (green dot at μ_I = 0 eV), Pb-rich (blue dot at μ_{Pb} = 0 eV), and the intermediate case (purple dot), respectively.

In the case of TFA and Ac we also include FATFA, FAAc and $Pb(TFA)_2$, $Pb(Ac)_2$ in our analysis, in particular we are interested whether these phases are more stable than Ac or TFA in the gas phase. Thus, first we reorder (4):

$$\frac{1}{2}\mu_{H^2} = \mu_{FA} - \mu_{FA-H} \#(6)$$

Then we can arrange the chemical potential of μ_{TFA-H} for the free form as:

$$\mu_{TFA-H} = \mu_{TFA} - \frac{1}{2}\mu_{H_2} \#(7)$$

Then from the FAX (X=Ac,TFA) source:

$$\mu_{TFA-H} = \mu_{FAX} - \mu_{FA} \#(8)$$ From the $Pb(X)_2$ (X=Ac,TFA) source:

$$\mu_{TFA-H} = \frac{\mu_{Pb(X)_2} - \mu_{Pb}}{2} \#(9)$$

We assumed that the gas-phase μ_{TFA} and μ_{Ac} are the upper limit and thus only use the FAX source when $\mu_X < 0$ similar to condition (5) above. In practice we found that the FAX is almost always the best source, except in the iodine-rich cases where the gas-phase X is the better source. See Table S7 below.

Table S7. Chemical potentials calculated using DFT results and equations (1-9) described above. We embolden the chemical potential used for each regime in the case of μ_{TFA-H} and μ_{Ac-H} since in these cases different sources may be more stable in each case.

	I Rich	Moderate	Pb Rich
μ_{Pb}	-5.74	-4.76	-3.78
μ_{I}	-1.72	-2.21	-2.70
μ_{FA}	-45.63	-45.15	-44.66
	I Rich	Moderate	Pb Rich
$1/2\ \mu_{H^2}$ *FA Source*	-5.09	-4.60	-4.11
μ_{TFA-H} *Gas Phase*		**-44.08**	
μ_{TFA-H} *FATFA Source*	-43.83	**-44.32**	**-44.81**
μ_{TFA-H} *$Pb(TFA)_2$ Source*	-42.74	-43.23	-43.72
μ_{Ac-H} (Gas Phase)		**-43.38**	
μ_{Ac-H} *FATFA Source*	-43.37	**-43.86**	**-44.34**
μ_{Ac-H} *$Pb(TFA)_2$ Source*	-43.03	-43.52	-43.58

FAAc, FATFA, $Pb(Ac)_2$ and $Pb(TFA)_2$ phases used in this work (built & optimized).

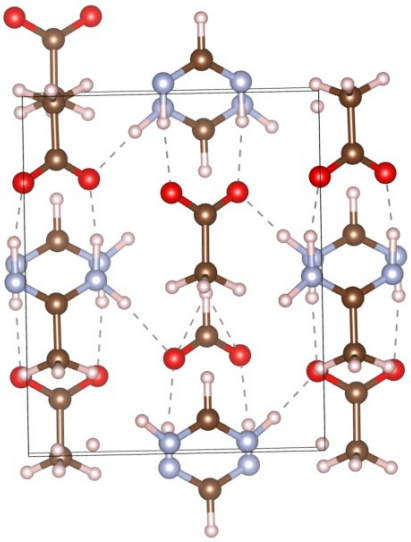

Fig. S38. Phase of FAAc, built by taking formamidinium formate and adding a methyl group to the formate [18].

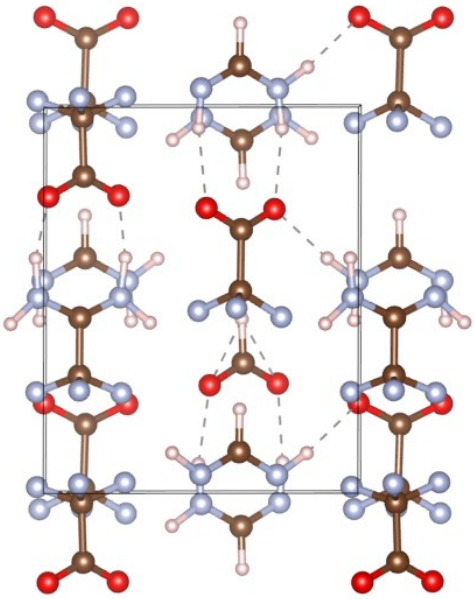

Fig. S39. Phase of FATFA constructed from FAAc by replacing hydrogen of Ac with fluorine.

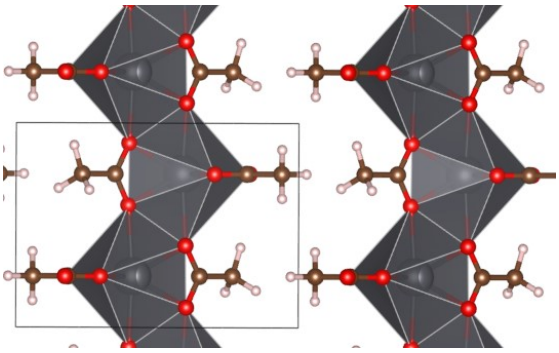

Fig. S40. Alpha-Pb$(Ac)_2$ found in literature [19] and optimized with DFT.

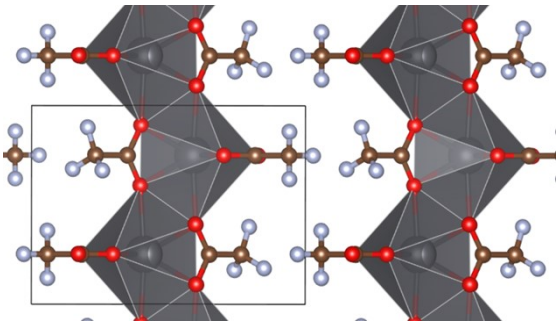

Fig. S41. Alpha-Pb$(TFA)_2$ built from Alpha-Pb$(Ac)_2$ by replacing hydrogens with fluorine.

DFT charge displacement diagrams

The surface charge density difference $\Delta\rho$ in each point of space divided into a FFT-grid and is defined as:

$$\Delta\rho(D^q) = \rho_{perovsk/pass}(D^q) - \rho_{perovsk}(D^q) - \rho_{pass} \quad (10)$$

Where $\rho_{perovsk/pass}$, $\rho_{perovsk}$, ρ_{pass} are the charge densities of the complex, the passivant-free surface and the passivant, respectively. We plot this quantity for the 2D-3D interfaces of FAPI with PEAI, PEAAc and PEATFA in Figure S8. Also we consider all three plane-averaged charge displacements projected onto the z-axis.

Work Function DFT analysis

In Table S8 we present the work function changes of the FAI-surface when PEAI, PEATFA or PEAAc is inserted into a Schottky defect. The Fermi energy change and work function change is very small; however, a useful observable can be observed from

the surface's charge displacement by calculating the change in the potential of the vacuum "above" the passivant when looking down the long z-axis (which includes the vacuum). For clarity we show a worked out example with V_I (hole acceptor) and V_{FA} (electron acceptor) in Fig. S38. Here we plot the Potential vs Distance (A) graphs using the pyband package. In the case of the pristine FAI-rich surface where both terminals are equivalent the potential remains flat in the vacuum (since no dipole is induced) ; however, the addition of a vacancy or passivant induces a net dipole moment thus shifting the potential and thus causing $dV/dz \neq 0$. Via a calculation of the slope of the shift dV/dz we can easily classify the passivants' general effect which is useful to know for general information.

Table S8. The calculated Fermi Energy, Work Function, change in work function ΔW (referenced to the pure supercell) and the change in the Coulombic Potential of the vacuum as well as the character of some representative defects and the passivated surface for the FAI-Rich Surface.

FAI-Rich Surface	3x3x5 , k111				Character
	E-fermi (eV)	Work Function (eV)	ΔW (eV)	dV/dz (e/ Å)	
Pure	-2.39	4.95	-	-	
V_{FA}	-2.82	5.40	0.46	4.99	Electron Acceptor
V_I	-0.53	3.05	-1.90	-8.65	Hole acceptor
V_{FAI}	-2.52	5.07	0.13	1.52	Electron Acceptor
Passivated					
$PEAI_{FAI}$	-2.40	4.98	0.03	-4.41	Hole Acceptor
$PEATFA_{FAI}$	-2.39	4.96	0.01	-2.82	
$PEAAc_{FAI}$	-2.37	4.93	-0.02	-6.89	

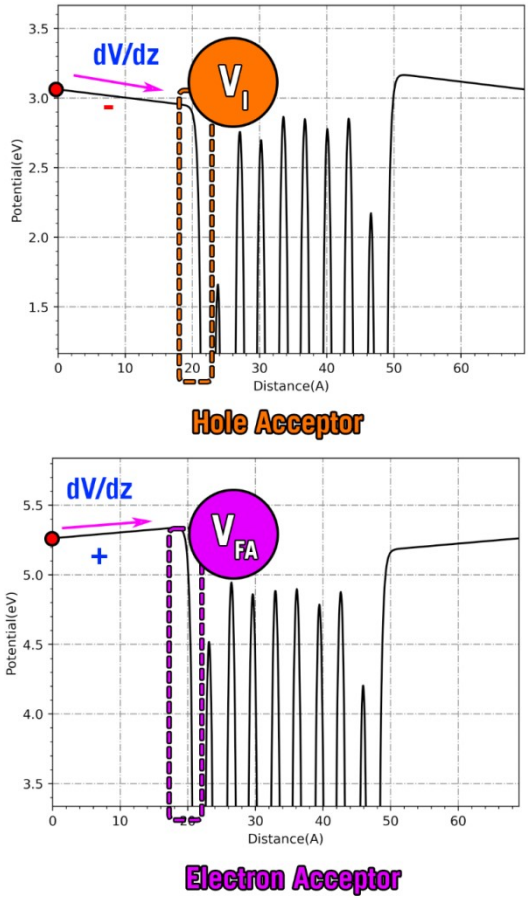

Fig. S42. The potential versus distance plots of the iodine vacancy (top) and FA vacancy (bottom) of the FAI-rich surface. The red dot indicate the points at which work function is determined. The arrow indicates the direction along which dV/dz is calculated.

References

1. Y. Zheng, X. Xu, S. Liu, G. Xu, Z. Bi, Y. Zhu, K. Wang, S. Liu, A. Guerrero and G. Xing, *Sol. RRL*, 2022, **6**, 2200737.
2. Y. Zhao, F. Ma, Z. Qu, S. Yu, T. Shen, H.-X. Deng, X. Chu, X. Peng, Y. Yuan, X. Zhang and J. You, *Science*, 2022, **377**, 531-534.
3. S. Tan, T. Huang, I. Yavuz, R. Wang, T. W. Yoon, M. Xu, Q. Xing, K. Park, D.-K. Lee, C.-H. Chen, R. Zheng, T. Yoon, Y. Zhao, H.-C. Wang, D. Meng, J. Xue, Y. J. Song, X. Pan, N.-G. Park, J.-W. Lee and Y. Yang, *Nature*, 2022, **605**, 268-273.
4. G. Kresse and J. Hafner, *Physical Review B*, 1994, **49**, 14251-14269.
5. J. P. Perdew, K. Burke and M. Ernzerhof, *Phys. Rev. Lett.*, 1996, **77**, 3865-3868.
6. S. Grimme, J. Antony, S. Ehrlich and H. Krieg, *The Journal of Chemical Physics*, 2010, **132**.
7. U.-G. Jong, C.-J. Yu, Y.-S. Kim, Y.-H. Kye and C.-H. Kim, *Physical Review B*, 2018, **98**, 125116.
8. H. Xue, G. Brocks and S. Tao, *Phys. Rev. Mater.*, 2021, **5**, 125408.
9. G. Kresse and D. Joubert, *Physical Review B*, 1999, **59**, 1758-1775.
10. P. E. Blöchl, *Physical Review B*, 1994, **50**, 17953-17979.

11. I. Płowaś-Korus and J. Kaczkowski, *New J. Chem.*, 2022, **46**, 15381-15391.
12. S. M. Park, M. Wei, J. Xu, H. R. Atapattu, F. T. Eickemeyer, K. Darabi, L. Grater, Y. Yang, C. Liu, S. Teale, B. Chen, H. Chen, T. Wang, L. Zeng, A. Maxwell, Z. Wang, K. R. Rao, Z. Cai, S. M. Zakeeruddin, J. T. Pham, C. M. Risko, A. Amassian, M. G. Kanatzidis, K. R. Graham, M. Grätzel and E. H. Sargent, *Science*, 2023, **381**, 209-215.
13. L. Kuai, Y. Wang, Z. Zhang, Y. Yang, Y. Qin, T. Wu, Y. Li, Y. Li, T. Song, X. Gao, L. Wang and B. Sun, *Sol. RRL*, 2019, **3**, 1900053.
14. A. Zohar, I. Levine, S. Gupta, O. Davidson, D. Azulay, O. Millo, I. Balberg, G. Hodes and D. Cahen, *ACS Energy Lett.*, 2017, **2**, 2408-2414.
15. X. Gao and X. Zhang, *Journal of Alloys and Compounds*, 2019, **810**, 151947.
16. P. Zhao, W. Yin, M. Kim, M. Han, Y. J. Song, T. K. Ahn and H. S. Jung, *J. Mater. Chem. A*, 2017, **5**, 7905-7911.
17. M. A. Reshchikov, G. C. Yi and B. W. Wessels, *Physical Review B*, 1999, **59**, 13176-13183.
18. Z. Zhou, R. A. Aitken, C. Cardinaud, A. M. Z. Slawin, H. Wang, A. M. Daly, M. H. Palmer and S. G. Kukolich, *The Journal of Chemical Physics*, 2019, **150**.
19. F. J. Martínez-Casado, M. Ramos-Riesco, J. A. Rodríguez-Cheda, F. Cucinotta, E. Matesanz, I. Miletto, E. Gianotti, L. Marchese and Z. Matěj, *Inorg. Chem.*, 2016, **55**, 8576-8586.